Influence of air-entraining agent and freeze-thaw action on pore structure in high-strength concrete by using CT-Scan technology

Dorys C. González[1,*], Álvaro Mena[1], Jesús Mínguez[1] and Miguel A. Vicente[1]

[1] University of Burgos, Dpt. Civil Engineering, C/ Villadiego s/n, 09001 Burgos, Spain.

* Correspondence: dgonzalez@ubu.es; Tel.: +34-947-25.94.20

Abstract

In this work, the effects caused by both the amount of air-entraining agent (AEA) and freeze-thaw cycles on microstructure of high-strength concrete have been analyzed. For this purpose, five series of concrete specimens have been manufactured, each of them containing a different amount of AEA. Then, all series have been subjected to up to 300 freeze-thaw cycles. In addition, the specimens have been analyzed using a computed tomography (CT) scan device at pre-defined freeze-thaw cycles and all data have been processed with digital image processing (DIP) software.

The results reveal, on the one hand, that the quantity of AEA has a greater influence on pore structure, and additionally the freeze-thaw action only slightly modifies the pore structure. As AEA increases, a progressive rise of the porosity and the number of pores is observed up to a maximum value. Next, a decrease is noticed. Moreover, there is not a linear relation between porosity and AEA. Furthermore, as AEA increases, a variation of its size and shape is observed. Alternatively, the effect of freeze-thaw cycles is more complex and does not show a monotonous tendency. The results reveal that the first 50 freeze-thaw cycles have the strongest influence on pore structure, observing a decrease in porosity. For the rest of the cycles, the porosity increases progressively resulting, after 300 freeze-thaw cycles, in a slightly lower porosity in almost all series than in those presented at the beginning. Hydration of unhydrated cement particles alongside with microcracking act

27   as opposite performances during the freeze-thaw cycles. Therefore, this can suggest that, under these conditions,

28   freeze-thaw action is not able to damage significantly the microstructure of concrete.

29   The results show that the series with a lower AEA content show a better behavior under freeze-thaw cycles.

30   In this case, the specimens exhibit a lower porosity and a higher level of small pores, and the pores evince a

31   more elongated shape. All these features lead to a more impermeable concrete and, therefore, with a better

32   performance under freeze-thaw cycles.

33

34   **Keywords:** computed tomography; air-entraining agent; freeze-thaw cycles; high-strength concrete; pore

35   structure; pore distribution.

36

1. Introduction

Freeze-thaw action has a determining influence on service life of concrete structures located in many cold regions of the planet. As temperature decreases below 0°C, the free water into concrete freezes and increases in volume, bringing along with it an increase in pressure. When temperature rises above 0°C, the free water returns to its original liquid form, leading to a decrease on the internal pressure. The repeated action of this freeze-thaw process cause, in concrete structures, the birth and growth of microcracks. This phenomenon, along with the action of external loads, can result in structural collapse (Kosior-Kazberuk, 2013; Ma et al., 2017; Shields et al., 2018). This nature of cumulative damage is the reason why this mechanism is also known as thermal fatigue.

Pores have a key role in the strength of concrete structures against freeze-thaw cycles; particularly in the water unsaturated ones. Their most direct influence lies in the fact that they act as a reserve of volume against water expansion when freezing. In this way, the unsaturated pores are able to reduce the internal pressure of concrete. Thus, it is common for structural standards in cold regions to require the use of AEA in concrete manufacturing with the aim of assuring a suitable freeze-thaw strength (ASTM C226-19, 2019; UNE-EN 206, 2018).

The role of AEA is to introduce air into the concrete matrix shaped like stable microbubbles, whose size is about one tenth of a millimeter (100 μm) (Jianxun et al., 2014). As a result, high porosity is achieved. However, porosity (defined as the ratio between the volume of trapped air and the total volume of concrete) is a global parameter that does not completely define the behavior of concrete under freeze-thaw cycles. In this sense, there is some recent research that highlights the key role of concrete microstructure (Dong et al., 2018; Han and Tian, 2018; Luo et al., 2017; Netinger Grubeša et al., 2019; Shields et al., 2018; Suzuki et al., 2017; Tian and Han, 2018). Therefore, it is interesting to study not only porosity, but also all the parameters related to pore structure (size, shape, distribution, etc.).

Pores also affect the response of concrete against mechanical stresses. A number of semi-empirical relationships between porosity and concrete strength can be found in scientific literature. The most remarkable ones are those belonging to Balshin (1949), Ryshkewitch (1953), Schiller (1958) and Hasselman (1963). In all of them, it is stablished that an increase in porosity involves a loss of compressive, tensile and flexural strength. In the case of mechanical fatigue, although its study is much more recent, a decrease in fatigue life while porosity increases has been observed (Chen et al., 2013; Vicente et al., 2018a).

The interaction between freeze-thaw cycles and mechanical response of concrete structures is of great interest. This phenomenon is observed in concrete bridges and concrete wind turbine towers located in regions subjected to thermal fatigue cycles, as in the north of USA and south of Canada, the north of Europe or China

68   and south of Russia, among others. In addition to thermal fatigue, these structures are subjected to external

69   loads of both static and dynamic nature, as well as to mechanical fatigue. In both cases, high-strength concrete

70   is commonly used.

71   As with thermal fatigue, mechanical fatigue results in a progressive degradation of the internal

72   microstructure of concrete (Fan and Sun, 2019; Skarżyński et al., 2019; Vicente et al., 2018b, 2018a). In

73   consequence, it is expected to find an addition of both the effects caused by the different types of fatigue,

74   resulting in the acceleration of the birth and growth of the microcracking, and a reduction of the service life of

75   the structure. However, few works thereon have been published so far, most of these focused on the study of

76   concrete pavements (Shen et al., 2018; Yang et al., 2018).

77   According to IUPAC, pores can be classified according to their size into micropores (smaller than 2 nm),

78   mesopores (from 2 to 50 nm) and macropores (larger than 50 nm) (Le et al., 2015; Rouquerol et al., 1994; Vydra

79   et al., 2001). The traditional methods to analyze the pore structure are nitrogen absorption and mercury-intrusion

80   porosimetry (MIP) (Gu et al., 2018; Netinger Grubeša et al., 2019), even though they have important limitations.

81   On the one hand, they can only provide the pore-size distribution, but neither their spatial distribution nor their

82   morphological parameters can be demonstrated. On the other hand, the information that they provide is related

83   to the open porosity and not to the close one, which is rather more interesting when studying this phenomenon.

84   Nowadays, the use of computed tomography (CT) scanning technology in the analysis of concrete

85   microstructure is increasingly common. In this field, there are many research works mainly focused on fiber-

86   reinforced concrete, in which several parameters concerning fiber distribution and orientation are analyzed (Gao

87   et al., 2018; González et al., 2018; Jasiūnienė et al., 2018; Oesch et al., 2018; Skarżyński and Suchorzewski,

88   2018; Miguel A. Vicente et al., 2019b). Additionally, in recent years computed tomography (CT) has begun to

89   be applied for the study of concrete pore morphology (Mínguez et al., 2019; Nitka and Tejchman, 2018;

90   Olawuyi and Boshoff, 2017; Zhao et al., 2019; Zhou et al., 2019).

91   CT-Scan technology is able to isolate all pores of any concrete specimen with a minimum size of about

92   10 μm; namely, macropores. Moreover, much information can be obtained about every single element: position,

93   volume, surface, length, etc. This way, statistical studies can be carried out with these parameters or even with

94   some previous obtained data, such as the shape factor, etc.

95   The aim of this work is to study the changes produced in the pore structure of high-strength concrete due

96   to two variables: the amount of AEA and the freeze-thaw action. For that purpose, concrete specimens with

97   different amounts of AEA have been casted, and then they have been subjected up to 300 freeze-thaw cycles.

98   Additionally, the specimens have been scanned by using a CT-scan at pre-defined number of cycles (0, 50, 100

99   and 300 cycles). The results obtained enable to define several correlations between the variables under study

100   and the evolution of concrete microstructure. High-strength concrete is commonly used in concrete bridges and

101   concrete wind turbine towers.

102   The innovation of this paper is the use of computerized tomography to study the variation of the porosity

103   of concrete subjected to freeze-thaw cycles. The computerized tomography allows the evaluation of many

104   parameters of the pores (much more than other methods commonly used for the measurement of porosity), such

105   as pore-size distribution, pore length and shape factor. These parameters can be therefore correlated to the

106   behavior of the specimen under freeze-thaw cycles, in order to investigate the impact of the microstructure on

107   their macroscopic response.

108   This paper is structured as follows. The experimental procedure is presented in Section 2; the results

109   obtained are described and discussed in Section 3; the correlation between internal microstructure and behavior

110   under freeze-thaw cycles is described in Section 4; and finally, the conclusions are found in Section 5.

111   **2. Experimental program**

112   *2.1. Materials*

113   In this research, 60 specimens divided in 5 series have been casted, which results in 12 specimens per

114   individual series. The only difference between each series is the amount of AEA, which has been gradually

115   increased from series A0.0 (0%) to series A0.4 (0.4%). The percentages of AEA have been chosen considering

116   that 0.3% is the maximum amount recommended by the AEA manufacturer. Table 1 shows the dosage of

117   concrete used in each series. As can be observed, some series show a quantity of AEA lower than the maximum

118   recommended, while series A0.4 shows an amount greater than the maximum recommended.

119   Portland cement with high initial strength CEM I 52.5 R was used together with siliceous fine aggregate

120   with a maximum size of 4 mm and coarse aggregate with a size between 4 and 6 mm. The AEA used was

121   MasterAir 100 (BASF, Ludwigshafen am Rhein, Germany). Finally, superplasticizer MasterGlenium 51

122   (BASF, Ludwigshafen am Rhein, Germany) and nanosilica MasterRoc MS 685 (BASF, Ludwigshafen am

123   Rhein, Germany) were used.

124

125

126

127

128

129   **Table 1.** Concrete mixture.

Dosage	A0.0	A0.1	A0.2	A0.3	A0.4
Cement (kg/m3)			700.0		
Water (kg/m3)			219.0		
Superplasticizer (kg/m3)			22.0		
Nanosilica (kg/m3)			10.0		
Fine Aggregate (kg/m3)			685.0		
Coarse Aggregate (kg/m3)			794.0		
Air Entraining Agent (kg/m3)	0.00	0.72	1.44	2.16	2.88
Ratio AEA/Cement	0.0%	0.1%	0.2%	0.3%	0.4%

130

131   The specimens tested are cubic with an edge of 40 mm, and they have been obtained from prismatic

132   specimens with a size of 40x40x160 mm. A 2.8 mm-thickness diamond disc has been used for the cut. A total

133   of 3 cubic specimens have been cut off from every prismatic specimen, so the ends of the prism have been

134   discarded (Figure 1).
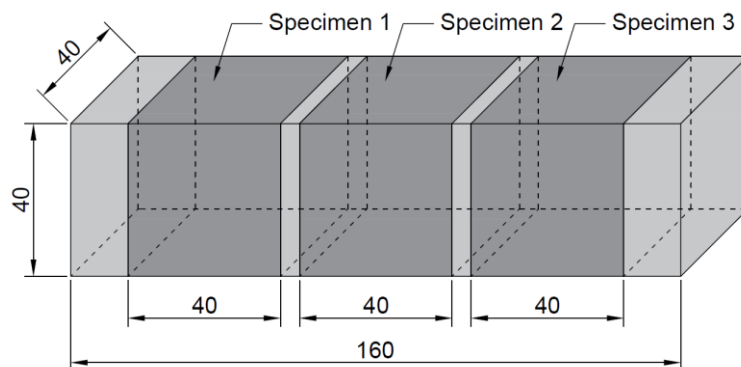
135

136   **Figure 1**. Cubic specimen extraction from prismatic specimen.

137   The specimens were cured for 90 days in a climatic chamber at a relative humidity of 97%±0.3% and an

138   ambient temperature of 20 °C ± 0.5 °C. All the specimens were approximately 90 days-old at the start of the

139   test campaign.

140   *2.2. Testing procedure*

141   Out of the 12 specimens of each series, 3 of them have been subjected to uniaxial compression test,

142   following the European standard UNE-EN 12390-3 (2020), in order to determine the average compression

143 strength of concrete (f_{cm}). Table 2 shows the results obtained, together with the standard deviation in brackets.

144 Besides, 9 specimens of each series have been subjected up to 300 freeze-thaw cycles, according to ASTM

145 C666/C666M-15 (2015) standard. The range of temperatures in every cycle is stablished between -18°C y 4°C,

146 and the tolerance of the equipment used is ±1°C. A freezing chamber with temperature monitoring has been

147 used during freezing, while a common cold store was used for thawing. Temperature has been systematically

148 controlled at the beginning and the end of every stage. The total duration of every freeze-thaw cycle was 2

149 hours, with both stages being equal (1 hour). However, as mentioned in the American standard, during the time

150 that it was not possible to continue with freeze-thaw cycles, the specimens were kept in frozen condition (-

151 18°C) to avoid the loss of moisture.

152 **Table 2.** Average compression strength of concrete and standard deviation.

| Series	f_{cm} (MPa)
A0.0	98.4 (1.5)
A0.1	99.8 (0.9)
A0.2	92.3 (3.2)
A0.3	88.6 (3.0)
A0.4	91.3 (2.7)

153

154 *2.3. CT scanning and image postprocessing*

155 Each specimen has been scanned four times: the first one before starting the freeze-thaw test and three

156 times during its development; more specifically, at 50, 100 and 300 cycles. The CT-scan used is a GE Phoenix

157 v|tome|x (General Electric, Boston, MA, USA) device. It is equipped with an X-ray tube of 300 kV/500 W. This

158 facility includes a software that provides sectional images of the specimens with a resolution of 2048x2048

159 pixels. Both the pixel size and the spacing between consecutive slices is 35 μm, so the voxel size (volumetric

160 pixel) is 35x35x35 μm^3. Thus, a total of 1334 images can be obtained from each specimen.

161 The software included in the CT-scan works with 8-bit images, so a grey value in a range varying from 0

162 to 255 is assigned to each voxel, where 0 means black and 255 means white. The value assigned depends on

163 the linear attenuation coefficient μ of the material, which in turn depends on density. Therefore, light grey

164 voxels (high values) belong to more dense points, while dark grey voxels (low values) belong to less dense

165 points. For instance, pores are shown in black since they are filled with air, whose density is very low. Finally,

166 as a result of the scanning process, a matrix including X, Y and Z coordinates of the center of gravity of each

167 voxel as well as its grey value is obtained. The total number of voxels per specimen is approximately $1.7 \cdot 10^9$.

168 The average scanning time of each specimen is about 1 hour. More detailed information regarding computed

169 tomography can be found in (Miguel A Vicente et al., 2019; Vicente et al., 2017, 2014).

170   Next, image postprocessing has been carried out using the digital image processing (DIP) software AVIZO

171 (FEI Visualization Sciences Group, Hillsboro, OR, USA). This tool enables identification and isolation of each

172 individual pore into the specimens. First, the software identifies the voxels belonging to pores, which are the

173 ones whose grey values are under the threshold value. With the aim of selecting a suitable threshold value, the

174 histograms of grey distribution of all specimens have been studied. As a result, it is concluded that a grey value

175 of 28 fits reasonably well into the pore-matrix interface. Figure 2 shows an example of a histogram of grey

176 distribution, in which the threshold value of 28 is highlighted.
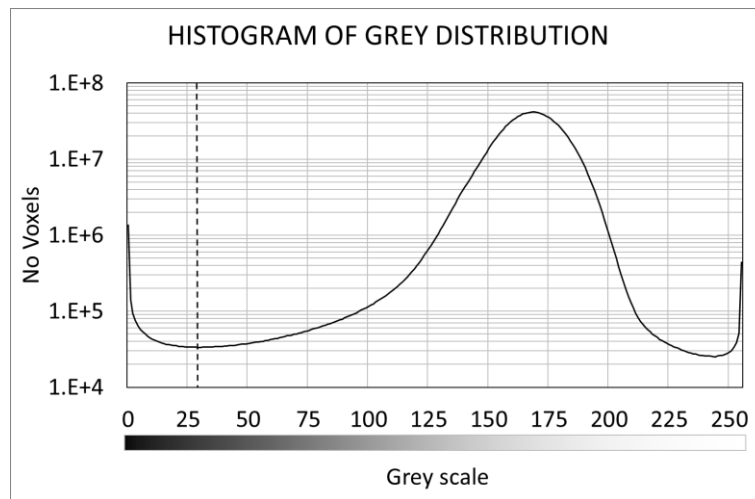

178 **Figure 2**. Example of a histogram of grey distribution. The threshold grey value (28) is highlighted in dotted

179 line, so voxels with a grey value between 0 and 28 are considered as pores.

180   As illustrated in Figure 2, a grey value of 28 corresponds to the minimum of the histogram function. This

181 means that this grey value corresponds to the border between the holes (darker voxels and more habitual) and

182 the concrete matrix (whiter voxels, and also more common). Considering all voxels with a grey value below

183 28, it is guaranteed that the entire volume of each pore is captured.

184   After that, the DIP software merges the voxels in contact, creating groups that correspond to the pores into

185 the concrete specimens. Figure 3 shows the pores identified and isolated in one specimen of each series. Finally,

186 many data of every individual pore can be obtained: X, Y and Z coordinates of the center of gravity, as well as

187 its volume, surface, length, etc. The length of a pore is defined as the maximum distance between two voxels

188 belonging to the same pore. In this work, only pores equal to or greater than 0.1 mm have been considered; that

189 is, with more than 3 voxels in their largest direction. The remaining ones have been discarded since their

190 parameters cannot be determined with sufficient accuracy. The results shown are the average values of the 9

191 specimens of each series. In all cases, the variability between samples belonging to the same series was very

192 low.

(a) (b) (c)

(d) (e)
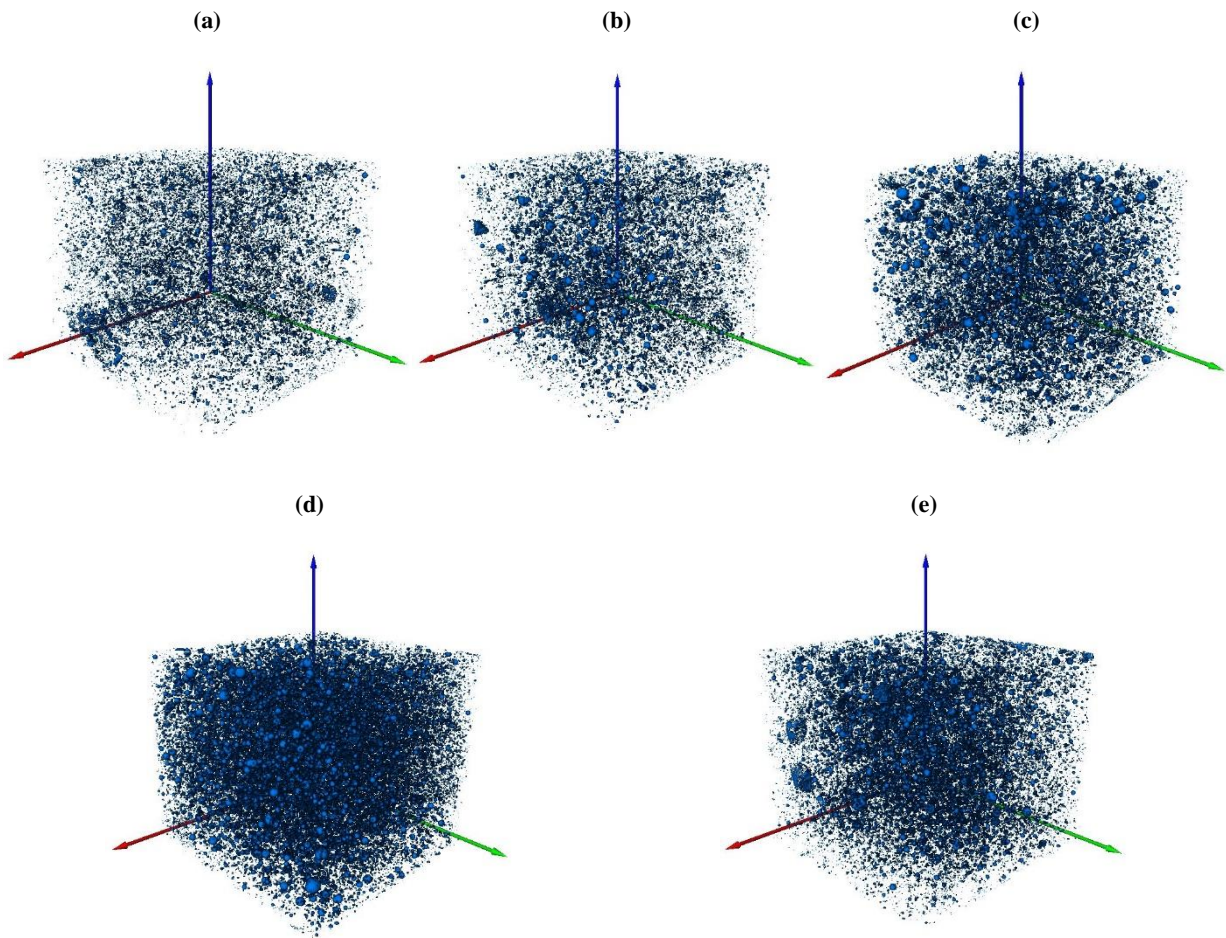
193 **Figure 3**. 3D reconstructed images of pore distribution in specimens of series A0.0 (a), A0.1 (b), A0.2 (c), A0.3 (d) and

194 A0.4 (e). They were obtained after 100 freeze-thaw cycles.

3. Results and discussion

196 As a result of the CT scanning and the subsequent postprocessing through the DIP software, a large amount

197 of information about every individual pore is obtained. In order to study the pore structure depending on the

198 amount of AEA and the freeze-thaw action, an in-depth analysis has been carried out, focused on the most

199 interesting parameters. In this case, a global study of pore-size distribution has been developed first, and then

200 several particular analyses about two significant parameters – length and shape factor – have been carried out.

201 *3.1. Pore-size distribution*

202 Two different types of curves are commonly used to analyze the pore-size distribution. Firstly, the porosity

203 curves relate the size of each pore with the porosity that the smaller pores represent. Therefore, porosity is

204   displayed in the ordinate axis, defined as the ratio between the volume of pores considered (V_p) and the volume

205   of the specimen (V_s) (Eq. (1)).

$$p = \frac{V_p}{V_s} \tag{1}$$

206   Secondly, the cumulative pore-volume curves relate the size of each pore with the relative volume of the

207   smaller pores. Thus, relative pore-volume is displayed in the ordinate axis, defined as the ratio between the

208   volume of pores considered (V_p) and the total volume of pores of the specimen ($V_{p,tot}$) ((Eq. (2)).

$$V_{p,rel} = \frac{V_p}{V_{p,tot}} \tag{2}$$

209   Figures 4 and 5 show the porosity curves and the cumulative pore-volume curves, respectively. All series

210   have been plotted in both graphs, also considering the effect of freeze-thaw cycles. The values shown in Figures

211   4 and 5 correspond to the average values of each series.

212   In Figure 4, it is clearly observed that the amount of AEA has a decisive influence on concrete

213   microstructure in general and on porosity in particular. When only the 0-cycle curves are compared, it is noticed

214   that series A0.0, which does not contain any AEA, has the lower porosity. The addition of AEA causes an

215   increase in porosity, as expected, until the maximum dosage recommended by the manufacturer is reached,

216   which in this case corresponds with series A0.3. From then on, a decrease in porosity is observed (Table 3).

217   These results match with those belonging to other investigations in which the influence of AEA on concrete

218   porosity is also analyzed (Kim et al., 2012; Vicente et al., 2018a).

219   **Table 3.** Initial porosity (0 freeze-thaw cycles).

| Series	Porosity (%)	Pore density (mm^{-3})	Maximum pore size, D_{90} (mm)
A0.0	0.43	0.73	1.32
A0.1	0.45	0.73	1.49
A0.2	1.49	1.13	2.62
A0.3	1.78	1.24	2.42
A0.4	1.11	0.99	1.85

220

221   With the aim of understanding the causes that explain the increase in porosity with the amount of AEA,

222   the results in Table 3 and Figure 5 can be referred. Firstly, Table 3 reveals that pore density (defined as the

223   number of pores per mm^3) increases with AEA, which means that the number of pores also does. Secondly, the

224   maximum pore size (D_{90}) can be obtained from the cumulative pore-volume curves (Figure 5), defined as the

225 size that is only exceeded by 10% of the total pores. It is a parameter often used to characterize the pore-size

226 distribution of a specimen. The maximum pore size of each series at 0 freeze-thaw cycles is presented in Table

227 3. An increase in its value is observed with the amount of AEA, which implies that the pore size also increases.

228 This fact is also observed in Figure 5 through a displacement of the cumulative pore-volume curves to the right.

(a) **(b)**

(c) **(d)**

(e)
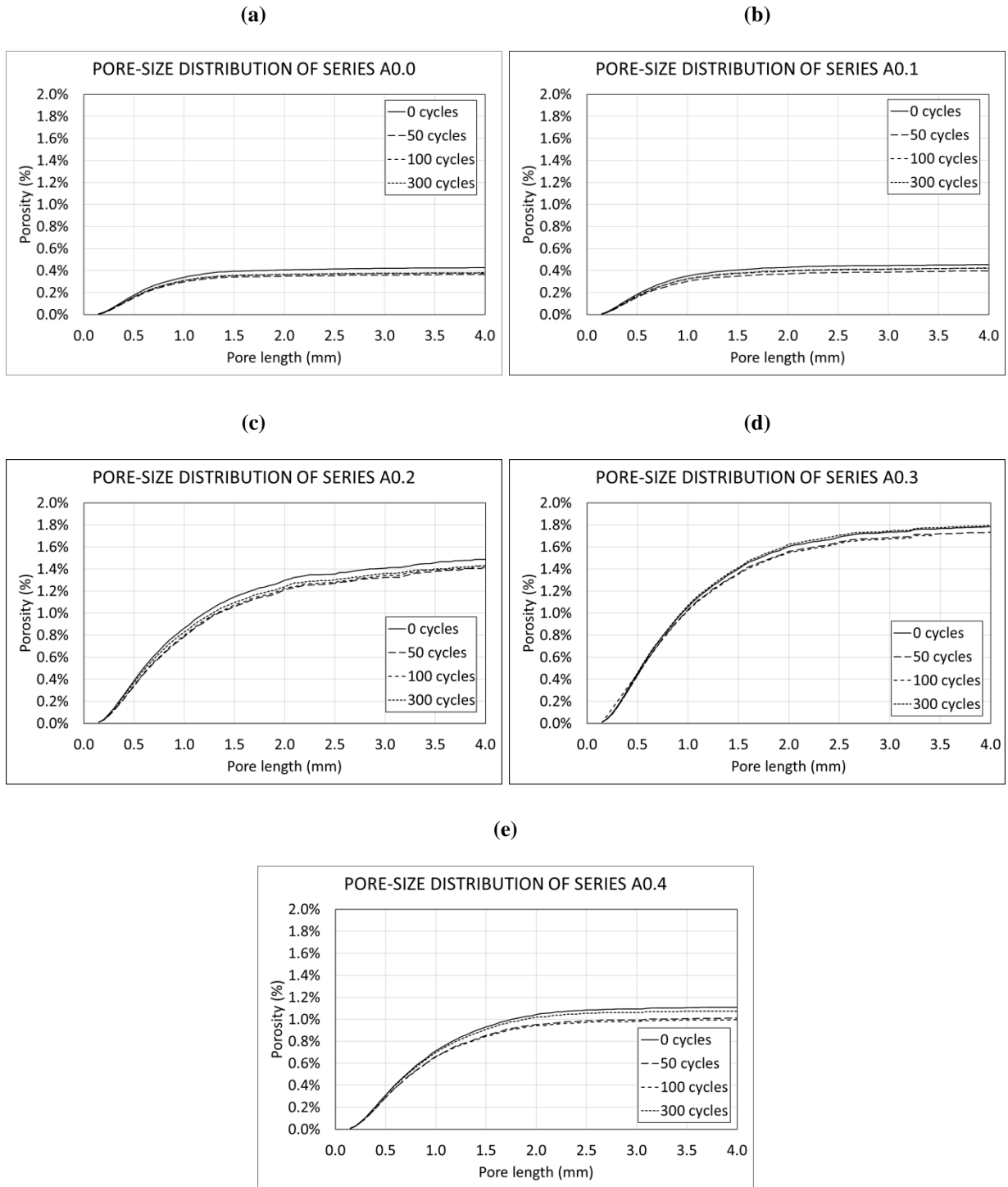
229 **Figure 4**. Porosity curves of series A0.0 (a), A0.1 (b), A0.2 (c), A0.3 (d) and A0.4 (e).

230

(a)

(b)

(c)

(d)

(e)
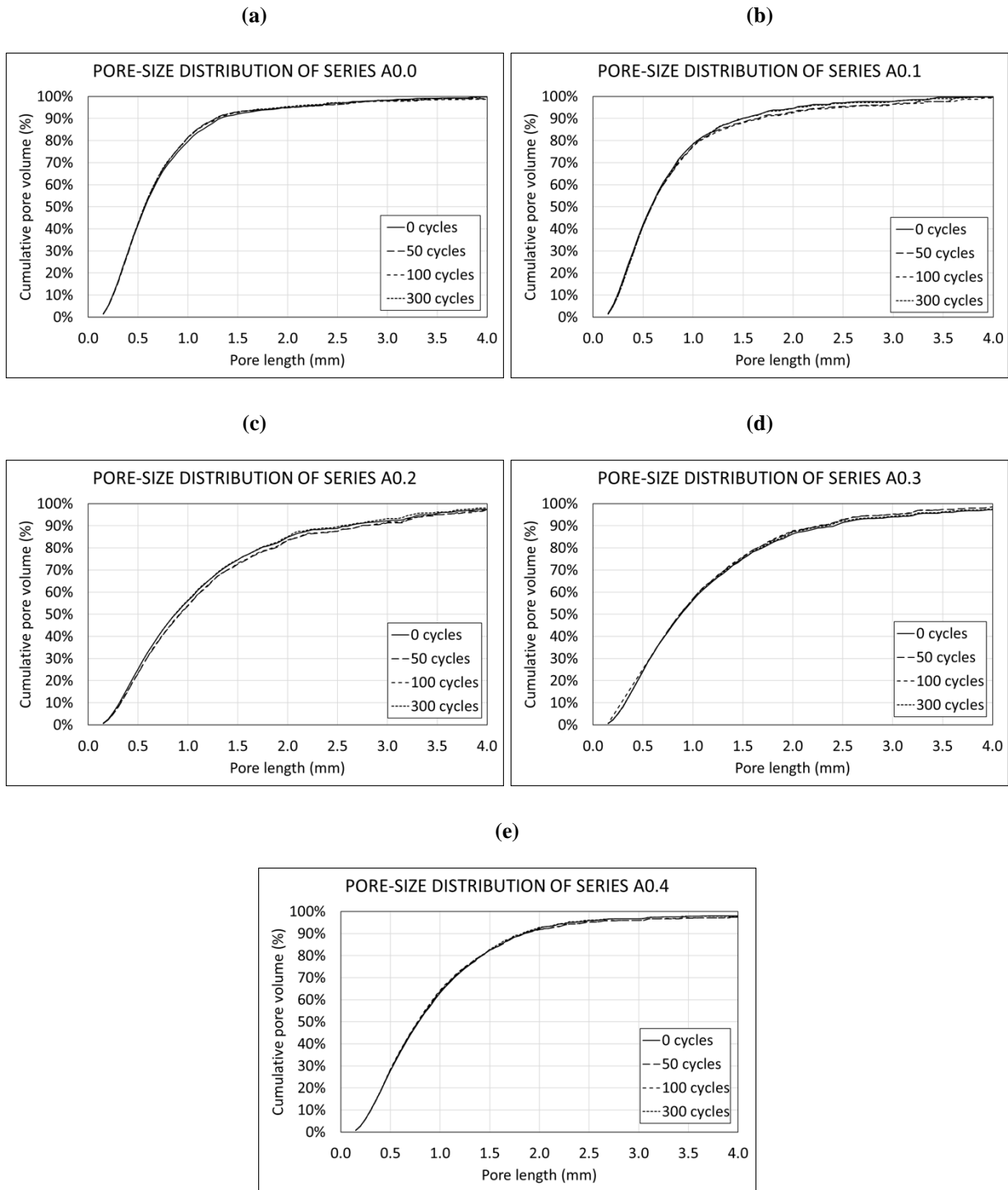
231   **Figure 5**. Cumulative pore-volume curves of series A0.0 (a), A0.1 (b), A0.2 (c), A0.3 (d) and A0.4 (e).

232   Consequently, the results reveal that the increase of the porosity is because the AEA not only generates

233   more pores, but also larger ones.

234   It is noticed that negligible quantities of AEA do not produce a significant increase in porosity. This could

235   be because of the size of the pores generated not being big enough to be detected by the CT-scan; in this case,

236   under 100 μm. However, as the quantity of AEA increases, stable pores of increasing size are created. Therefore,

237 there is necessarily a percentage limit of AEA for which the size of the pores generated is above the minimum

238 that can be detected by the CT-scan. This fact has two clear consequences. On the one hand, with very low

239 contents of AEA, the porosity measured is almost identical to that belonging to a specimen without AEA. On

240 the other hand, with slightly higher contents, the volume of air initially trapped into non-detectable pores is now

241 considered, hence causing a sudden rise in porosity. In this case, the percentage limit of AEA is placed between

242 0.1% and 0.2%, which explains the dramatic increase in porosity between series A0.1 and A0.2 (Table 3).

243 Finally, when the amount of AEA is too large, the size of the pores increases and therefore the upward force on

244 them also does. This way, the pore retention capacity inside the concrete matrix decreases, the air is released

245 and hence the porosity decreases. This explains what happens in series A0.4. These results agree with those

246 found by other researchers (Abd Elrahman et al., 2020; Mendes et al., 2017).

247 On the other side, Figure 4 reveals that freeze-thaw action has a much smaller influence on pore structure

248 than the amount of AEA. However, it is worth highlighting some phenomena that are repeated in all series.

249 Firstly, it is observed that the initial 50 cycles are those showing the greatest impact on concrete microstructure,

250 causing a decrease in porosity. This aspect is more noticeable in the series with more quantity of AEA; in

251 particular, in series A0.4 the reduction in porosity reaches 0.1%. Consequently, a densification of the concrete

252 matrix occurs, which could mean an improvement of its mechanical response. Secondly, over the remaining

253 250 cycles a gradual recovery of porosity is observed. Again, this increase is greater in the series with higher

254 amount of AEA; in fact, series A0.3 is the only one whose final porosity (after 300 freeze-thaw cycles)

255 overcomes the initial one (with 0 cycles).

256 When comparing the curves of 300 cycles of all the series, it is observed that, in most of the series, the

257 curve for 300 cycles is below the curves for 0 cycles. On the contrary, in series A0.3, the curve for 300 cycles

258 is above the curve for 0 cycles. However, this variation is small, which means that, in this case, the impact of

259 the freeze-thaw cycles on the concrete matrix is not relevant. This agrees with the visual observation of the

260 specimens at the end of the freeze-thaw cycles process; they did not show apparent signs of damage.

261 Moreover, Figure 5 reveals that the freeze-thaw action has a very low influence on pore size variations,

262 since cumulative pore-volume curves remain almost unchanged.

263 These changes in porosity due to freeze-thaw cycles can be explained by the action of two opposite

264 mechanisms. First, a hydration of the cement particles that had not reacted occurs. In the case of high-strength

265 concrete, water/cement ratios often used are very low and a fraction of cement particles remain non-hydrated

266 and, simultaneously, small water bubbles are retained. In addition, the freeze-thaw test conditions, with the

267 specimens completely submerged in water, facilitate the access of water inside concrete. Therefore, local

cement hydration reactions are expected to occur, bringing with them an rise in volume of solids and a decrease in porosity. Secondly, the freeze-thaw action results in internal damage inside concrete matrix. This is because during freezing hydraulic pressure on pore-matrix interface significantly increases. If concrete does not have enough tensile strength to withstand this internal pressure, microcracks appear. Consequently, an increase in the total empty space inside the specimens (equivalent to porosity) occurs.

During the first 50 freeze-thaw cycles, a predominance of the hydration mechanism over the microcracking is observed, and hence a global decrease in porosity is produced. Thereafter, non-hydrated cement particles are residual, while the damage caused by freeze-thaw progressively increases. However, this second mechanism is not clearly observed in series A0.0 and A0.1, where the amount of AEA is lower.
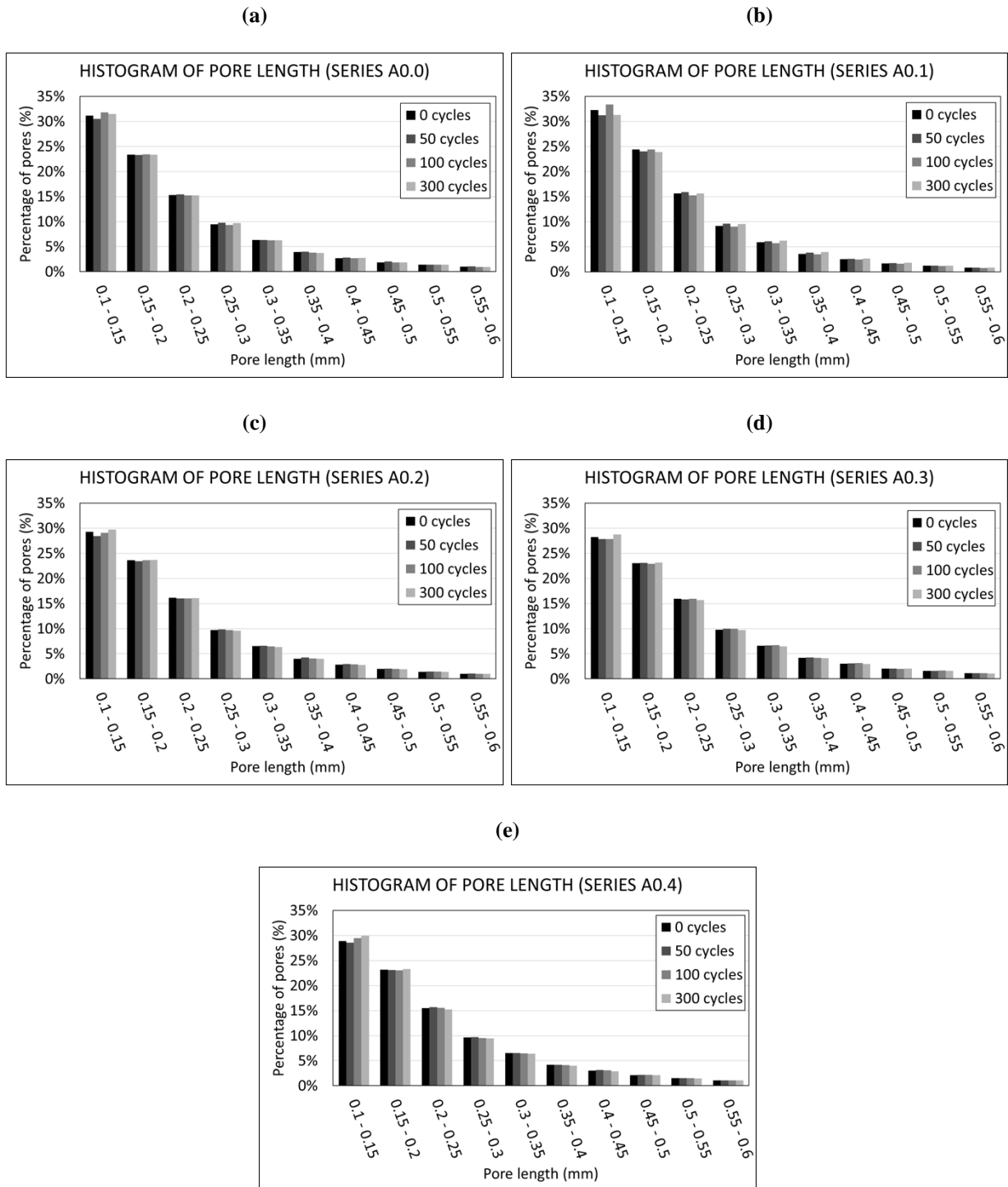
3.2. Histogram of pore length

On the basis of the values of length of each individual pore, the histograms of pore length can be plotted. They are graphs that correlate a particular range of pore lengths with the percentage that represents over the total number of pores. These histograms are shown in Figure 6, where it is also included the evolution due to freeze-thaw action. As explained in Section 2, the pores whose length is lower than 0.1 mm have been discarded, since they cannot be defined with enough accuracy or even, they may correspond to digital noise because of the scanning process itself.

Figure 6 reveals that the percentage of pores in all series decreases as the length increases, following a clear negative exponential trend. In fact, pores whose length is between 0.1 and 0.2 mm represent more than 50% of the total pores in all cases.

In addition, other aspects can be outlined in this figure. Firstly, the influence of AEA content is much lower than in porosity curves. However, it seems that its effect continues to be greater than the one belonging to freeze-thaw cycles. If only the 0-cycle bars are taken into account in order to discard the effect of thermal fatigue, it is noticed that the percentage of the smallest pores (0.1-0.2 mm) decreases with the increase in AEA. As a result, the percentage of the remaining pore sizes (0.2-0.6 mm) increases. This is explained by the fact that, as the amount of AEA increases, the pore size also does. Nevertheless, this trend is not repeated in series A0.4, the one containing the largest amount of AEA. As explained above, the reason behind is that, under very high contents of AEA, the pore retention capacity decreases, releasing the entrained air and reducing the porosity.

(a)   **(b)**

(c)   **(d)**

(e)

Figure 6. Histogram of pore length of series A0.1 (a), A0.1 (b), A0.2 (c), A0.3 (d) and A0.4 (e).

Secondly, it is noticed that the effect of the freeze-thaw cycles is less significant. A clear tendency is not observed in series A0.0 and A0.1. On the contrary, it seems that in the rest of series the initial 50 cycles reduce the percentage of the smallest pores (0.1-0.2 mm). However, during the rest of cycles a recovery of those pores occurs; in fact, the final percentage of small pores is even higher than the initial one. The aforementioned mechanisms can be used to explain this behavior. During the initial freeze-thaw cycles, local cement hydration reactions predominate. As a result, concrete expansion takes place, which is more likely to affect the smallest

305   pores, closing them and falling in number. Likewise, the internal damage caused by the freeze-thaw cycles

306   predominates over the rest of time. This damage results in microcollapses which disaggregate the pore-matrix

307   interface and, with regard to the CT-scan, this can be read as the division in smaller pores, or even the defects

308   created can be under the detection threshold of the device.

309   *3.3. Histogram of shape factor*

310   One interesting geometrical parameter to characterize pore structure can be obtained from the data

311   provided by both the CT-scan and the DIP software. This is the shape factor, defined as the ratio between the

312   volume of a pore and the volume of the sphere circumscribed to that pore (Eq. (3)) (Blott and Pye, 2008):

$$SF = \frac{V_p}{\frac{1}{6} \cdot \pi \cdot L_p^3} \tag{3}$$

313   where V_p is the pore volume and L_p is the pore length.

314   Histograms of shape factor can be plotted by using the data of the shape factor of each individual pore.

315   They consist on graphs that correlate a particular range of shape factors with the percentage that represents over

316   the total number of pores. These histograms are shown in Figure 7, where it is also included the evolution due

317   to freeze-thaw cycles. It should be highlighted that shape factors ranging from 0.8 to 1 are not included, since

318   they represent a very small proportion and do not add any relevant information.

319   A first conclusion drawn from the histograms in Figure 7 is that pores are not spherical at all, since their

320   shape factors are far from 1. In particular, the modal value varies between 0.2 and 0.4, so the shape of the pores

321   is rather elongated or irregular. This matches with the findings of other recent investigations (Chandrappa and

322   Biligiri, 2018; Vicente et al., 2019a).

323   Secondly, an increase in shape factor with the amount of AEA is observed; in other words, as the content

324   of AEA increases, pores become more spherical. Moreover, the histograms are flattened simultaneously, which

325   implies a reduction in peak percentages. This suggests that, though the shape factor of the pores increases, it

326   does not tend to stabilize around a certain value. This growth can be explained due to the fact that AEA is able

327   to introduce stable pores inside concrete, whose shape factors are relatively high. This way, the irregularity of

328   pores in the no-AEA situation (series A0.0) is compensated, resulting in higher shape factors. Finally, the trend

329   is reversed in series A0.4 and the shape factor of pores decreases. As explained before, under very high contents

330   of AEA, the pores retention capacity decreases and hence they are released. Therefore, as precisely these

331   microbubbles have a high shape factor, the final result is that pore sphericity is reduced.

332
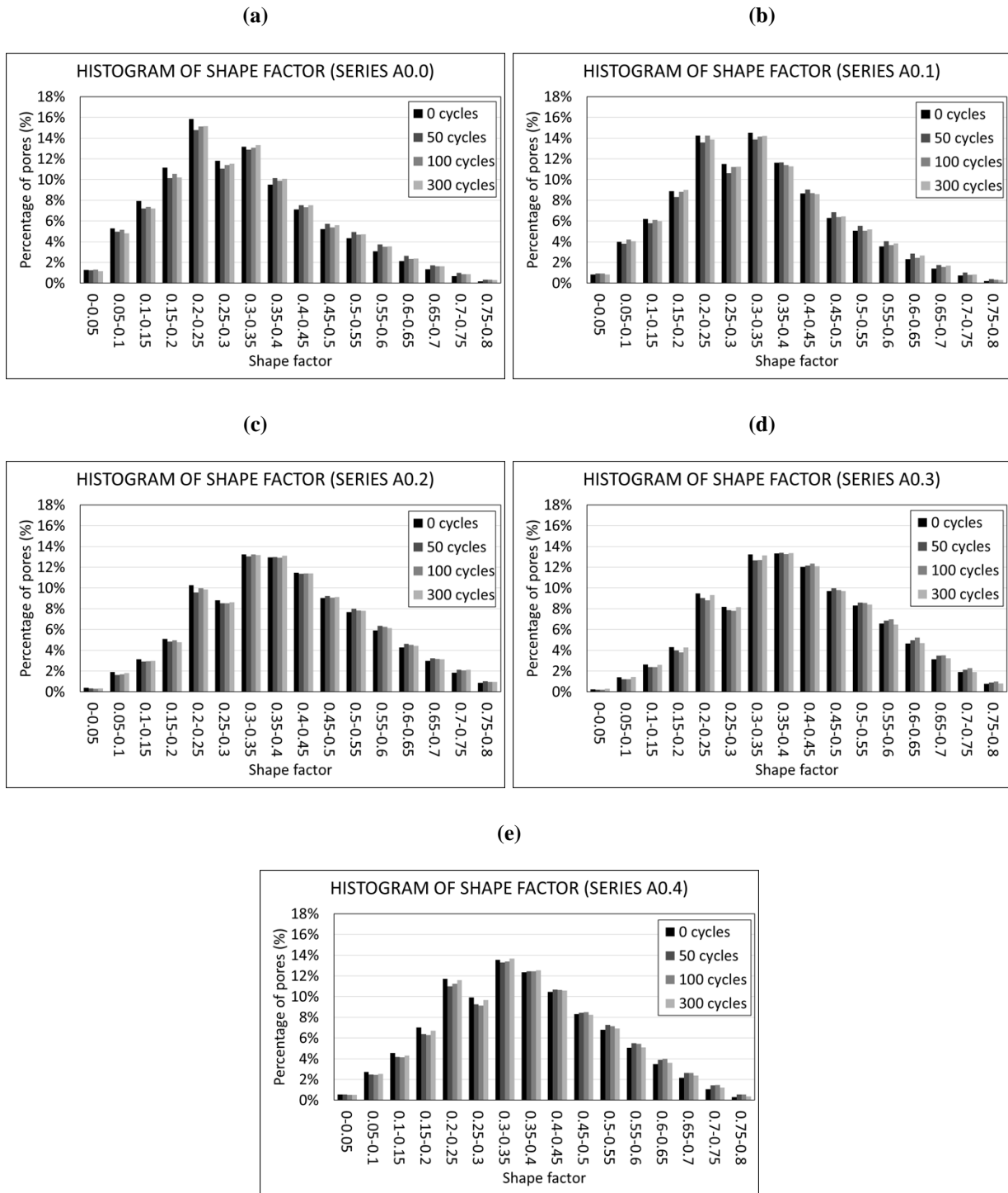
Figure 7. Histogram of shape factor of series A0.0 (a), A0.1 (b), A0.2 (c), A0.3 (d) and A0.4 (e).

Lastly, it is observed that freeze-thaw action barely modifies the shape factor of pores. However, as mentioned above, it seems that the initial 50 cycles have a determining influence. During this period, an increase in shape factor in all series occurs, which is particularly significant in the series with the least content of AEA (series A0.0 and A0.1). This is reflected in a slightly displacement of the histograms to the right. Then, over the rest of the cycles a progressive decrease in shape factor is noticed, and finally the resulting shape factors are very similar to the initial ones. Again, this behavior can be explained due to both the hydration and freeze-thaw

340 damage mechanisms. During the first cycles, local cement hydration reactions cause a concrete expansion that

341 mainly affects the smallest pores, closing them. These pores tend to be precisely more elongated or irregular,

342 thus an increase in shape factor occurs. In the case of the series with larger amounts of AEA, as the pores

343 introduced cause by themselves an increase in shape factor, the effect of hydration mechanism is less relevant.

344 Therefore, the increase in shape factor is lower. Finally, over the rest of cycles, freeze-thaw action causes

345 microcollapses in pores that modify them, making them more irregular or even subdividing them in smaller

346 pores also of irregular shape. In consequence, shape factor decreases.

347 **4. Correlation between internal microstructure and response under freeze-thaw cycles**

348 When the series of 0 cycles and of 300 cycles are compared globally, some trends are observed that can

349 help to understand the relationship between microstructure and macroscopic response.

350 In the series A0.0 and A0.1 it is observed that the porosity curves at 50, 100 and 300 cycles (Figure 4) are

351 very close to each other, which means that during the first freeze-thaw cycles a densification occurs but, finally,

352 the freeze-thaw cycles do not result in a global damage of the microstructure.

353 These series have some particular characteristics. First, the porosity in all of them is lower than in the rest

354 of the series. In addition, they initially have a percentage of pores between 0.1 and 0.15 mm higher than the

355 rest. In addition, the maximum pore size is clearly lower. The series A0.0 and A0.1 also show a distribution

356 curve of the shape factor different from the rest of the series. In these cases, the most common range is 0.20-

357 0.25, while for the rest of the series the most common range is clearly higher.

358 In summary, it is observed that the A0.0 and A0.1 series show the best behavior under freeze-thaw cycles,

359 which are characterized by having less porosity, smaller pores (which are specified in a higher percentage of

360 smaller pores and a smaller maximum pore size) and more elongated pores (with a smaller shape factor).

361 Apparently, the first freeze-thaw cycles cause a microcracking of the structure, helping to hydrate the

362 cement particles that had not yet been hydrated and ultimately resulting in a reduction in porosity. This process

363 consumes the free water that was inside the specimen. As concrete has low porosity and the pores are small, the

364 entry of water from the outside is very small, that it, they are almost waterproof, so there is less internal damage

365 caused by freeze-thaw cycles.

366 The series A0.2, A0.3 and A0.4 show a worse behavior under freeze-thaw cycles. By having more

367 porosity, the entry of water from the outside is greater (they are permeable), so the damage caused by freeze-

368 thaw cycles is greater. In addition, they show a higher percentage of larger pores, and also pores with less

369 elongated shapes (larger shape factor). This results in higher values of tensile stresses in the concrete matrix

370 around the pores, caused by the expansion of water when it frozen. It seems that the pores created by the AEA,

371 which tend to be more spherical as explained above, are more vulnerable to the freeze-thaw cycles.

372 **5. Conclusions**

373 In this work, the changes produced in the pore structure of high-strength concrete as a result of the amount

374 of AEA and freeze-thaw cycles are analyzed. For this reason, specimens with five different amounts of AEA

375 have been casted, and then they have been subjected up to 300 freeze-thaw cycles. The specimens have been

376 also scanned using a computed tomography scan at some pre-defined numbers of cycles. The most interesting

377 results are next summarized.

378 The amount of AEA has a determining influence on porosity. As its content increases, porosity also does,

379 but up to a limit. In this case, that limit is reached in series A0.3, which corresponds to the maximum dosage

380 recommended by the manufacturer. In addition, it is proved that the increase in porosity is due to the fact that

381 AEA is able to generate a greater number of pores and also larger pores. Regarding the reduction in porosity

382 with large amounts of AEA, it is explained because the pore retention capacity inside the concrete matrix

383 decreases.

384 Freeze-thaw action has less influence on porosity than the amount of AEA. Nevertheless, several

385 interesting phenomena are observed. It is noticed that the initial 50 cycles are those showing the most relevant

386 impact on pore structure, causing a decrease in porosity. However, over the rest 250 cycles a partial recovery

387 of porosity occurs. The final result is that porosity after 300 freeze-thaw cycles is slightly lower in all cases,

388 except for series A0.3, where it remains almost equal. This finding suggests that, under this type of concrete

389 and these test conditions, freeze-thaw action does not substantially damage concrete microstructure. This is

390 clearer in the case of series A0.0 and A0.1, with a lower content of AEA. In these series, the recovery of the

391 porosity after the initial 50 cycles is hardly observed.

392 The histograms of pore length show that the percentage of pores decreases with increasing length in all

393 series, following a clear negative exponential tendency. On the other side, it seems that the percentage of the

394 smallest pores (0.1-0.2 mm) decreases as the amount of AEA increases, while the rest of pore sizes (0.2-0.6

395 mm) increases. The reason is that AEA makes larger pores. With regard to the effect of freeze-thaw cycles, it

396 is observed that the first 50 cycles reduce the percentage of the smallest pores (0.1-0.2 mm), which is later

397 recovered over the remaining cycles. Behind this behavior, two opposite mechanisms could be found: concrete

398 hydration and freeze-thaw internal damage.

399   From the histograms of shape coefficient, it is concluded that pores are not spherical at all, but rather

400   elongated or irregular. In addition, an increase in shape factor with the amount of AEA is observed, which can

401   be explained because the pores generated by AEA are very stable, with a relatively high shape factor. Finally,

402   it is noticed again that the initial 50 freeze-thaw cycles are those which have the greatest influence on pore

403   structure, causing an increase in shape factor.

404   To sum up, the addition of AEA in concrete mixtures not only affects porosity, but also has a significant

405   impact on pore structure, causing an increase in the number of pores, their size and their shape factor.

406   Alternatively, it seems that freeze-thaw action causes an initial reduction in porosity, which afterwards is

407   gradually recovered. This recover is hardly observed in A0.0 and A0.1 series, with the lowest AEA content,

408   while it is clearly observed in the rest of the series.

409   In the end, the overall result is that porosity after 300 freeze-thaw cycles decreases slightly in almost all

410   series. Thus, suggesting that freeze-thaw cycles do not damage significantly the microstructure of concrete.

411   The best response under freeze-thaw cycles is provided by the A0.0 and A0.1 series, since the final porosity

412   is clearly smaller than the initial one. A lower porosity, smaller pores and more elongated pores characterize

413   these series. The first freeze-thaw cycles produce microcracking, which allows the hydration of cement particles

414   that have not been hydrated yet and, consequently, reduce porosity. During the rest of the freeze-thaw cycles,

415   the entry of water from the outside is (modest, limited) small, since concrete has low porosity and the pores are

416   small. Concrete is rather waterproof and, in consequence, the internal damage caused by freeze-thaw cycles is

417   exiguous.

418   **6. Acknowledgments**

421   **References**

422   Abd Elrahman, M., El Madawy, M.E., Chung, S.-Y., Majer, S., Youssf, O., Sikora, P., 2020. An Investigation

423   of the Mechanical and Physical Characteristics of Cement Paste Incorporating Different Air Entraining

424   Agents   using   X-ray   Micro-Computed   Tomography.   Crystals   10,   23.

425   https://doi.org/10.3390/cryst10010023

426   ASTM C226-19, Standard Specification for Air-Entraining Additions for Use in the Manufacture of Air-

427   Entraining Hydraulic Cement, ASTM International, USA, 2019. https://doi.org/10.1520/C0226-19

428   ASTM C666/C666M-15, Standard Test Method for Resistance of Concrete to Rapid Freezing and Thawing,

429   ASTM International, USA, 2015. https://doi.org/10.1520/C0666_C0666M-15

430   Balshin, M.Y., 1949. Relation of mechanical properties of powder metals and their porosity and the ultimate

431   properties of porous metal-ceramic materials. Dokl Akad Nauk SSSR 67(5).

432   Blott, S.J., Pye, K., 2008. Particle shape: a review and new methods of characterization and classification.

433   Sedimentology 55, 31–63. https://doi.org/10.1111/j.1365-3091.2007.00892.x

434   Chandrappa, A.K., Biligiri, K.P., 2018. Pore structure characterization of pervious concrete using X-ray

435   microcomputed tomography. J. Mater. Civ. Eng. 30, 1–11. https://doi.org/10.1061/(ASCE)MT.1943-

436   5533.0002285

437   Chen, Y., Wang, K., Wang, X., Zhou, W., 2013. Strength, fracture and fatigue of pervious concrete. Constr.

438   Build. Mater. 42, 97–104. https://doi.org/10.1016/j.conbuildmat.2013.01.006

439   Dong, Y., Su, C., Qiao, P., Sun, L., 2018. Microstructural damage evolution and its effect on fracture behavior

440   of concrete subjected to freeze-thaw cycles. Int. J. Damage Mech. 27, 1272–1288.

441   https://doi.org/10.1177/1056789518787025

442   Fan, Z., Sun, Y., 2019. Detecting and evaluation of fatigue damage in concrete with industrial computed

443   tomography technology. Constr. Build. Mater. 223, 794–805.

444   https://doi.org/10.1016/j.conbuildmat.2019.07.016

445   Gao, J., Sha, A., Wang, Z., Hu, L., Yun, D., Liu, Z., Huang, Y., 2018. Characterization of carbon fiber

446   distribution in cement-based composites by Computed Tomography. Constr. Build. Mater. 177, 134–147.

447   https://doi.org/10.1016/j.conbuildmat.2018.05.114

448 González, D.C., Mínguez, J., Vicente, M.A., Cambronero, F., Aragón, G., 2018. Study of the effect of the fibers'

449 orientation on the post-cracking behavior of steel fiber reinforced concrete from wedge-splitting tests and

450 computed tomography scanning. Constr. Build. Mater. 192, 110–122.

451 https://doi.org/10.1016/j.conbuildmat.2018.10.104

452 Gu, C., Sun, W., Guo, L., Wang, Q., Liu, J., Yang, Y., Shi, T., 2018. Investigation of Microstructural Damage

453 in Ultrahigh-Performance Concrete under Freezing-Thawing Action. Adv. Mater. Sci. Eng. 2018, 1–9.

454 https://doi.org/10.1155/2018/3701682

455 Han, N., Tian, W., 2018. Experimental study on the dynamic mechanical properties of concrete under freeze-

456 thaw cycles. Struct. Concr. 19, 1353–1362. https://doi.org/10.1002/suco.201700170

457 Hasselman, D.P.H., 1963. Relation Between Effects of Porosity on Strength and on Young's Modulus of

458 Elasticity of Polycrystalline Materials. J. Am. Ceram. Soc. 46, 564–565. https://doi.org/10.1111/j.1151-

459 2916.1963.tb14615.x

460 Jasiūnienė, E., Cicėnas, V., Grigaliūnas, P., Rudžionis, Ž., Navickas, A.A., 2018. Influence of the rheological

461 properties on the steel fibre distribution and orientation in self-compacting concrete. Mater. Struct. Constr.

462 51. https://doi.org/10.1617/s11527-018-1231-y

463 Jianxun, C., Xizhong, Z., Yanbin, L., Xianghui, D., Qin, L., 2014. Investigating freeze-proof durability of C25

464 shotcrete. Constr. Build. Mater. 61, 33–40. https://doi.org/10.1016/j.conbuildmat.2014.02.077

465 Kim, H.K., Jeon, J.H., Lee, H.K., 2012. Workability, and mechanical, acoustic and thermal properties of

466 lightweight aggregate concrete with a high volume of entrained air. Constr. Build. Mater. 29, 193–200.

467 https://doi.org/10.1016/j.conbuildmat.2011.08.067

468 Kosior-Kazberuk, M., 2013. Variations in fracture energy of concrete subjected to cyclic freezing and thawing.

469 Arch. Civ. Mech. Eng. 13, 254–259. https://doi.org/10.1016/j.acme.2013.01.002

470   Le, H.T., Kraus, M., Siewert, K., Ludwig, H.-M., 2015. Effect of macro-mesoporous rice husk ash on

471   rheological properties of mortar formulated from self-compacting high performance concrete. Constr.

472   Build. Mater. 80, 225–235. https://doi.org/10.1016/j.conbuildmat.2015.01.079

473   Luo, Q., Liu, D., Qiao, P., Feng, Q., Sun, L., 2017. Microstructural damage characterization of concrete under

474   freeze-thaw action. Int. J. Damage Mech. 27, 1–18. https://doi.org/10.1177/1056789517736573

475   Ma, Z., Zhao, T., Yang, J., 2017. Fracture Behavior of Concrete Exposed to the Freeze-Thaw Environment. J.

476   Mater. Civ. Eng. 29, 04017071. https://doi.org/10.1061/(ASCE)MT.1943-5533.0001901

477   Mendes, J.C., Moro, T.K., Figueiredo, A.S., Silva, K.D. do C., Silva, G.C., Silva, G.J.B., Peixoto, R.A.F., 2017.

478   Mechanical, rheological and morphological analysis of cement-based composites with a new LAS-based

479   air   entraining   agent.   Constr.   Build.   Mater.   145,   648–661.

480   https://doi.org/10.1016/j.conbuildmat.2017.04.024

481   Mínguez, J., Vicente, M.A., González, D.C., 2019. Pore morphology variation under ambient curing of plain

482   and fiber-reinforced high performance mortar at an early age. Constr. Build. Mater. 198, 718–731.

483   https://doi.org/10.1016/j.conbuildmat.2018.12.010

484   Netinger Grubeša, I., Marković, B., Vračević, M., Tunkiewicz, M., Szenti, I., Kukovecz, Á., 2019. Pore

485   Structure as a Response to the Freeze/Thaw Resistance of Mortars. Materials (Basel). 12, 3196.

486   https://doi.org/10.3390/ma12193196

487   Nitka, M., Tejchman, J., 2018. A three-dimensional meso-scale approach to concrete fracture based on

488   combined   DEM   with   X-ray   μCT   images.   Cem.   Concr.   Res.   107,   11–29.

489   https://doi.org/10.1016/j.cemconres.2018.02.006

490   Oesch, T., Landis, E., Kuchma, D., 2018. A methodology for quantifying the impact of casting procedure on

491   anisotropy   in   fiber-reinforced   concrete   using   X-ray   CT.   Mater.   Struct.   Constr.   51.

492   https://doi.org/10.1617/s11527-018-1198-8

493   Olawuyi, B.J., Boshoff, W.P., 2017. Influence of SAP content and curing age on air void distribution of high

494   performance concrete using 3D volume analysis. Constr. Build. Mater. 135, 580–589.

495   https://doi.org/10.1016/j.conbuildmat.2016.12.128

496   Rouquerol, J., Avnir, D., Fairbridge, C.W., Everett, D.H., Haynes, J.H., Pernicone, N., Ramsay, J.D.F., Sing,

497   K.S.W., Unger, K.K., 1994. Recommendations for the characterization of porous solids (Technical

498   Report), Pure and Applied Chemistry. https://doi.org/10.1351/pac199466081739

499   Ryshkewitch, E., 1953. Compression Strength of Porous Sintered Alumina and Zirconia. J. Am. Ceram. Soc.

500   36, 65–68. https://doi.org/10.1111/j.1151-2916.1953.tb12837.x

501   Schiller, K.K., 1958. Porosity and strength of brittle solids (with particular reference to gypsum), in: Mechanical

502   Properties of Non-Metallic Brittle Materials. pp. 35–49.

503   Shen, A., Lin, S., Guo, Y., He, T., Lyu, Z., 2018. Relationship between flexural strength and pore structure of

504   pavement concrete under fatigue loads and Freeze-thaw interaction in seasonal frozen regions. Constr.

505   Build. Mater. 174, 684–692. https://doi.org/10.1016/j.conbuildmat.2018.04.165

506   Shields, Y., Garboczi, E., Weiss, J., Farnam, Y., 2018. Freeze-thaw crack determination in cementitious

507   materials using 3D X-ray computed tomography and acoustic emission. Cem. Concr. Compos. 89, 120–

508   129. https://doi.org/10.1016/j.cemconcomp.2018.03.004

509   Skarżyński, Ł., Marzec, I., Tejchman, J., 2019. Fracture evolution in concrete compressive fatigue experiments

510   based on X-ray micro-CT images. Int. J. Fatigue 122, 256–272.

511   https://doi.org/10.1016/j.ijfatigue.2019.02.002

512   Skarżyński, Ł., Suchorzewski, J., 2018. Mechanical and fracture properties of concrete reinforced with recycled

513   and industrial steel fibers using Digital Image Correlation technique and X-ray micro computed

514   tomography. Constr. Build. Mater. 183, 283–299. https://doi.org/10.1016/j.conbuildmat.2018.06.182

515   Suzuki, T., Shiotani, T., Ohtsu, M., 2017. Evaluation of cracking damage in freeze-thawed concrete using

516   acoustic emission and X-ray CT image. Constr. Build. Mater. 136, 619–626.

517   https://doi.org/10.1016/j.conbuildmat.2016.09.013

518   Tian, W., Han, N., 2018. Pore characteristics (>0.1 mm) of non-air entrained concrete destroyed by freeze-

519   thaw cycles based on CT scanning and 3D printing. Cold Reg. Sci. Technol. 151, 314–322.

520   https://doi.org/10.1016/j.coldregions.2018.03.027

521   UNE-EN 12390-3. Ensayos de hormigón endurecido. Parte 3: Determinación de la resistencia a compresión de

522   probetas, AENOR, Spain, 2020.

523   UNE-EN 206. Hormigón. Especificaciones, prestaciones, producción y conformidad, AENOR, Spain, 2018.

524   Vicente, Miguel A, González, D.C., Mínguez, J., 2019. Recent advances in the use of computed tomography in

525   concrete technology and other engineering fields. Micron 118, 22–34.

526   https://doi.org/10.1016/j.micron.2018.12.003

527   Vicente, M.A., González, D.C., Mínguez, J., 2014. Determination of dominant fibre orientations in fibre-

528   reinforced high-strength concrete elements based on computed tomography scans. Nondestruct. Test.

529   Eval. 29, 164–182. https://doi.org/10.1080/10589759.2014.914204

530   Vicente, M.A., González, D.C., Mínguez, J., Tarifa, M.A., Ruiz, G., Hindi, R., 2018a. Influence of the pore

531   morphology of high strength concrete on its fatigue life. Int. J. Fatigue 112, 106–116.

532   https://doi.org/10.1016/j.ijfatigue.2018.03.006

533   Vicente, Miguel A., Mínguez, J., González, D.C., 2019a. Variation of the pore morphology during the early age

534   in plain and fiber-reinforced high-performance concrete under moisture-saturated curing. Materials

535   (Basel). 12. https://doi.org/10.3390/ma12060975

536 Vicente, M.A., Mínguez, J., González, D.C., 2017. The Use of Computed Tomography to Explore the

537 Microstructure of Materials in Civil Engineering: From Rocks to Concrete, in: Mesrur-Halefoğlu, A.

538 (Ed.), Computed Tomography. Advanced Applications. IntechOpen, pp. 207–229.

539 https://doi.org/10.5772/intechopen.69245

540 Vicente, Miguel A., Ruiz, G., González, D.C., Mínguez, J., Tarifa, M., Zhang, X., 2019b. Effects of fiber

541 orientation and content on the static and fatigue behavior of SFRC by using CT-Scan technology. Int. J.

542 Fatigue 128, 105178. https://doi.org/10.1016/j.ijfatigue.2019.06.038

543 Vicente, M.A., Ruiz, G., González, D.C., Mínguez, J., Tarifa, M., Zhang, X., 2018b. CT-Scan study of crack

544 patterns of fiber-reinforced concrete loaded monotonically and under low-cycle fatigue. Int. J. Fatigue

545 114, 138–147. https://doi.org/10.1016/j.ijfatigue.2018.05.011

546 Vydra, V., Vodák, F., Kapičková, O., Hošková, Š., 2001. Effect of temperature on porosity of concrete for

547 nuclear-safety structures. Cem. Concr. Res. 31, 1023–1026. https://doi.org/10.1016/S0008-

548 8846(01)00516-6

549 Yang, X., Shen, A., Guo, Y., Zhou, S., He, T., 2018. Deterioration mechanism of interface transition zone of

550 concrete pavement under fatigue load and freeze-thaw coupling in cold climatic areas. Constr. Build.

551 Mater. 160, 588–597. https://doi.org/10.1016/j.conbuildmat.2017.11.031

552 Zhao, Y., Wang, X., Jiang, J., Zhou, L., 2019. Characterization of interconnectivity, size distribution and

553 uniformity of air voids in porous asphalt concrete using X-ray CT scanning images. Constr. Build. Mater.

554 213, 182–193. https://doi.org/10.1016/j.conbuildmat.2019.04.056

555 Zhou, H., Li, H., Abdelhady, A., Liang, X., Wang, H., Yang, B., 2019. Experimental investigation on the effect

556 of pore characteristics on clogging risk of pervious concrete based on CT scanning. Constr. Build. Mater.

557 212, 130–139. https://doi.org/10.1016/j.conbuildmat.2019.03.310

UNIVERSITY OF BURGOS.
Department of Civil Engineering

Ph.D. Dorys González.
Dpto. Ingeniería Civil. University of Burgos.
c/ Villadiego s/n. 09001. Burgos. Spain
E-Mail: dgonzalez@ubu.es

Burgos. Sunday, 01 August 2021

Dear Editor,

I declare that this paper and the research shown in it has no conflict of interest.

Sincerely,

AUTHORSHIP STATEMENT

MANUSCRIPT TITLE:

Influence of air-entraining agent and freeze-thaw action on pore structure in high-strength concrete by using CT-Scan technology.

AUTHORS:

Dorys C. González (DCG), Álvaro Mena (AM), Jesús Mínguez, (JM), Miguel A. Vicente (MAV)

All persons who meet authorship criteria are listed as authors, and all authors certify that they have participated sufficiently in the work to take public responsibility for the content, including participation in the concept, design, analysis, writing, or revision of the manuscript.

Furthermore, each author certifies that this material or similar material has not been and will not be submitted to or published in any other publication before its appearance in the journal "Cold Regions Science and Technology".

Category 1

Conception and design of study: DCG, AM, JM, MAV.

Acquisition of data: AMA, JM

Analysis and/or interpretation of data: DCG, MAV.

Category 2

Drafting the manuscript: AM, JM, DCG

Revising the manuscript critically for important intellectual content: DCG, MAV

Category 3

Approval of the version of the manuscript to be published (the names of all authors must be listed): DCG, AM, JM, MAV.